

Geothermal implications for fracture-filling hydrothermal precipitation



L. Griffiths^{a,*}, M.J. Heap^a, F. Wang^a, D. Daval^b, H.A. Gilg^c, P. Baud^a, J. Schmittbuhl^a, A. Genter^d

^a Institut de Physique de Globe de Strasbourg, Université de Strasbourg/EOST, CNRS UMR 7516, 5 rue René Descartes, 67084 Strasbourg, France

^b Laboratoire d'Hydrologie et de Géochimie de Strasbourg, Université de Strasbourg/EOST, CNRS UMR 7517, 1 rue Blessig, 67084 Strasbourg, France

^c Lehrstuhl für Ingenieurgeologie, Technische Universität München, Arcisstr. 21, 80333 Munich, Germany

^d ES-Géothermie, 3 Chemin du Gaz, 67500 Haguenau, France

ARTICLE INFO

Article history:

Received 3 February 2016

Received in revised form 7 June 2016

Accepted 9 June 2016

Keywords:

Geothermal reservoir
Soultz-sous-Forêts
Buntsandstein
Permeability
Fracture sealing
Barite

ABSTRACT

In geothermal reservoirs, fluid circulation is greatly dependent on the geometry, density, and hydraulic properties of fractures. The Soultz-sous-Forêts geothermal site located in the Upper Rhine Graben in Alsace, France, consists of a granitic basement overlain by a 1.4 km-thick sedimentary succession. Core analysis and borehole wall imagery collected from reconnaissance well EPS1, drilled vertically to a depth of 2230 m, revealed an extensive fracture network throughout the granite and overlying sediments, including both open fractures and fractures sealed through mineral precipitation (primarily quartz, illite, chlorite, calcite, dolomite, barite, pyrite and galena). Here we present a combined experimental and modelling study that aims to provide insights into the permeability anisotropy in the Triassic Buntsandstein sandstone (1–1.4 km depth) and the impact of mineral precipitation. We targeted borehole samples that best represented the variability of fractures within the Buntsandstein. Forty cylindrical samples (40 mm in length and 20 mm in diameter) were prepared from the chosen borehole samples such that they contained sealed or partially-sealed fractures either parallel or perpendicular to their axis. We also prepared samples of the intact host rock. These samples were then subject to porosity and permeability measurements, and thin sections were made for Scanning Electron Microscopy (SEM) to characterise the nature of the fractures and the precipitated minerals. Permeability measurements of the Buntsandstein host rock yielded values ranging from 10^{-15} m² to less than 10^{-18} m². SEM and X-ray powder diffraction analyses suggest that prevalent pore-filling illitic clays can explain the low permeability of the sandstone host rock. Additionally, we found that the permeability of fractures depends on the nature of the filling and the extent of sealing, with barite providing the most effective precipitate. Taking into account the geothermal fluid composition at Soultz-sous-Forêts, we employ a kinetic model for the barite crystal growth rate with temperature to provide an estimate for the time scale over which open fractures can seal through barite precipitation (from months to days depending on temperature). The rate increases dramatically as the temperature of the geothermal brine decreases, highlighting the risk of mineral precipitation at geothermal sites, where fluid temperature fluctuates due to circulation through the reservoir rock and fluid mixing around the injection well. An improved knowledge of the time dependency of fracture permeability will provide insights into the permeability anisotropy in the Buntsandstein and may have repercussions for the geothermal exploitation and for the ongoing fluid flow modelling of the Soultz-sous-Forêts geothermal reservoir.

© 2016 Elsevier Ltd. All rights reserved.

1. Introduction

Fluid circulation in geothermal reservoirs is susceptible to the geometry and hydraulic properties of fractures (Grant and Bixley, 2011). The Soultz-sous-Forêts Enhanced Geothermal System (EGS) is located in the Upper Rhine Graben in Alsace, France, and consists of a granitic basement overlain by a 1.4 km-thick sedimentary suc-

* Corresponding author.

E-mail address: luke.griffiths@unistra.fr (L. Griffiths).

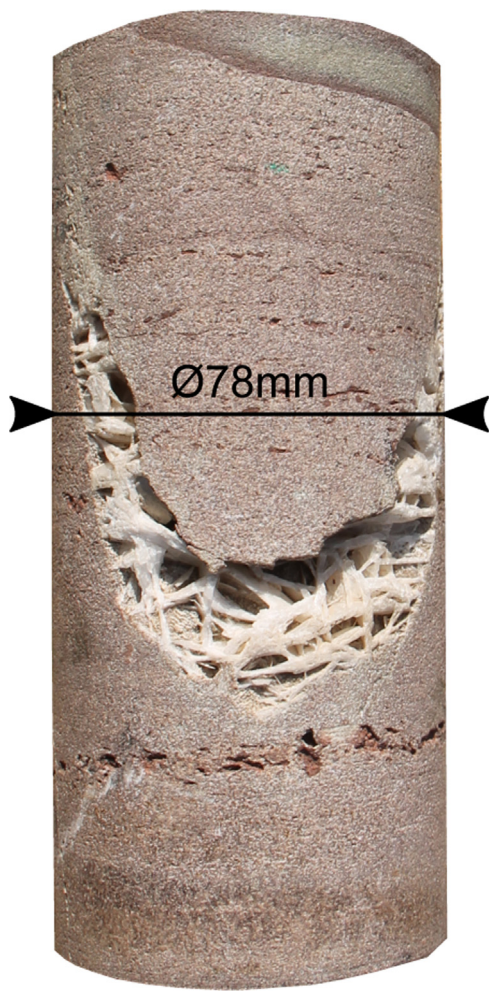


Fig. 1. Photo of a fractured Buntsandstein core sample from exploration well EPS1 at 1374 m depth. The rock contains a large fracture of roughly 1 cm in width, filled with precipitated barite crystals.

cession (Kappelmeyer and Gerard, 1989; Baria et al., 1999). This is a site of significant geothermal potential due to the high thermal gradient in the first 1 km of the sedimentary cover ($\sim 100^\circ\text{C}/\text{km}$) and the abundance of natural brines (Gérard et al., 2006; Genter et al., 2010). These brines have a high salinity, containing total dissolved solids of around 100 g/L and circulate over several kilometres, facilitating heat transfer (Sanjuan et al., 2010). Exploiting this natural heat source involves the use of deep wells and the fracture network in the granitic basement. The fracture network in the granite has been extensively studied (Dezayes et al., 2010; Genter and Traineau, 1996; Ledésert et al., 1993; Sausse et al., 2010; Surma and Géraud, 2003) as it is the target for two EGS heat exchangers at 3.5 and 5 km depth (Genter et al., 2010). In the Buntsandstein sandstone (1–1.4 km depth) and the granite below, the temperature gradient is lower ($\sim 30^\circ\text{C}/\text{km}$ and $\sim 5^\circ\text{C}/\text{km}$, respectively) than in the above sediments and has been linked to fluid convection (Pribnow and Clauer, 2000; Vidal et al., 2015). Numerical modelling of this hydrothermal convection at Soultz-sous-Forêts finds that the Buntsandstein, as well as the granite, plays an important role in controlling regional fluid flow (Guillou-Frottier et al., 2013; Magnenet et al., 2014).

Core analysis and borehole wall imagery collected from reconnaissance well EPS1 (Soultz-sous-Forêts), drilled vertically to a depth of 2230 m, reveal the geometry of an extensive fracture network throughout the granite and overlying sediments. This includes both open fractures and fractures filled through mineral

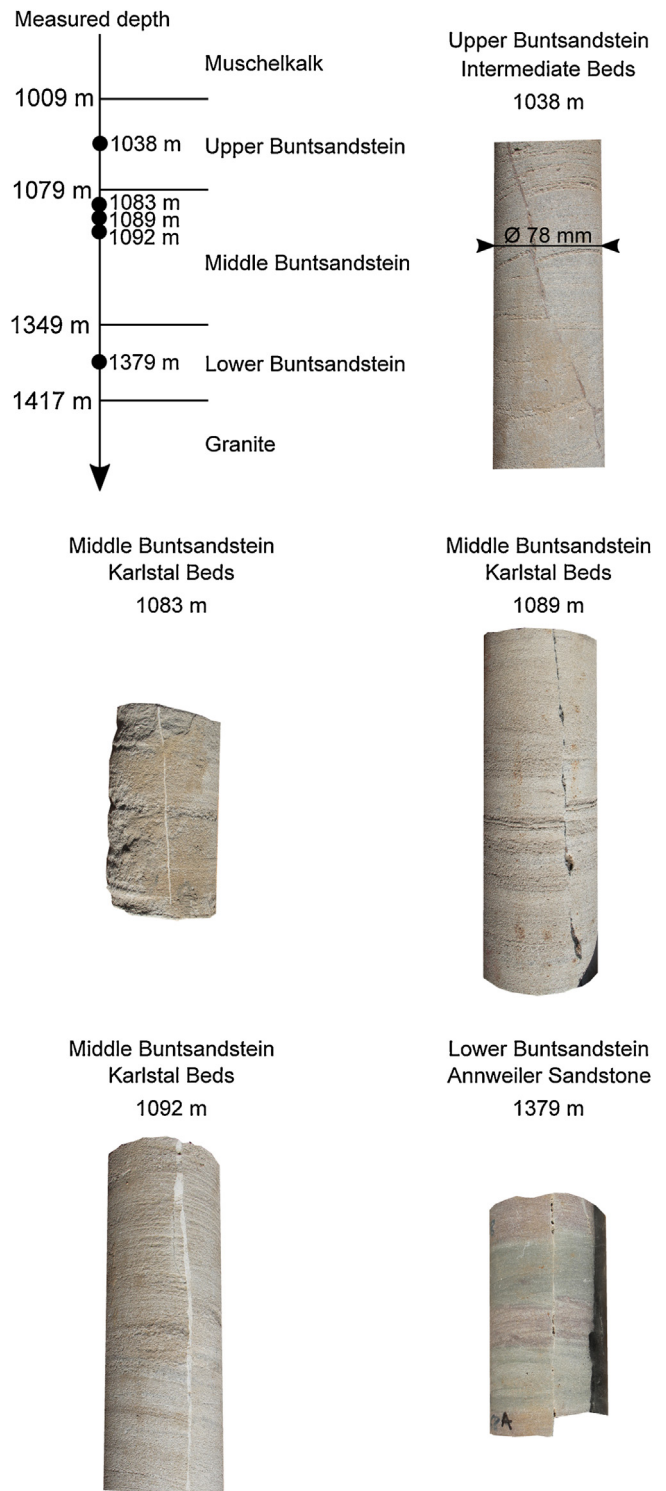


Fig. 2. Stratigraphy of and adjacent to the Buntsandstein, complete with the depths of the Formations (Muschelkalk, Upper, Middle, and Lower Buntsandstein, and the granite) and the depths of sampled cores from EPS1 (measured depths of 1038 m, 1083 m, 1089 m, 1092 m, and 1379 m). Photographs of the retrieved cores are also shown, which all contain sub-vertical sealed fractures with widths in the millimetre scale.

precipitation (primarily quartz, barite, calcite, and galena; Vernoux et al., 1995). EPS1 was continuously cored from 930 m to 2227 m measured depth and the granitic basement was reached at 1417 m (throughout this paper, all reported depths are measured depths). In the Buntsandstein (1000–1417 m depth in EPS1), core analysis

Table 1

Results of the X-ray powder diffraction analyses of the host rock at each investigation depth. Two samples of the 1038 m core were analysed due to its strong heterogeneity.

Measured depth (m)	Lithostratigraphy	Quartz (mass%)	Orthoclase (mass%)	Microcline (mass%)	Illite-Smectite (mass%)
1038	Upper Buntsandstein – Intermediate Beds	81	6	11	2
1083	Middle Buntsandstein – Karlstal Beds	91	3	5	1
1083	"	82	5	10	3
1089	"	87	5	6	2
1092	"	86	6	6	2
1379	Lower Buntsandstein – Annweiler Sandstone	63	5	12	20

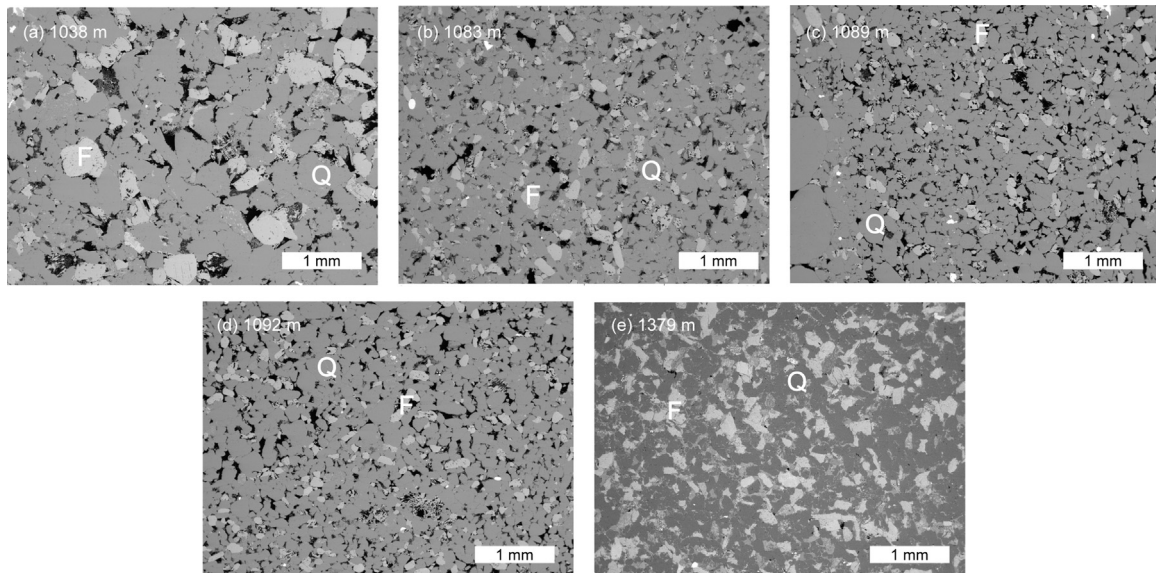


Fig. 3. SEM micrographs of thin sections of the intact rock from each core sample. These images show the intact host Buntsandstein at (a) 1038 m, (b) 1083 m, (c) 1089 m, (d) 1092 m, and (e) 1379 m depth. 'Q' and 'F' label the quartz and feldspar grains, respectively, and the porosity is black.

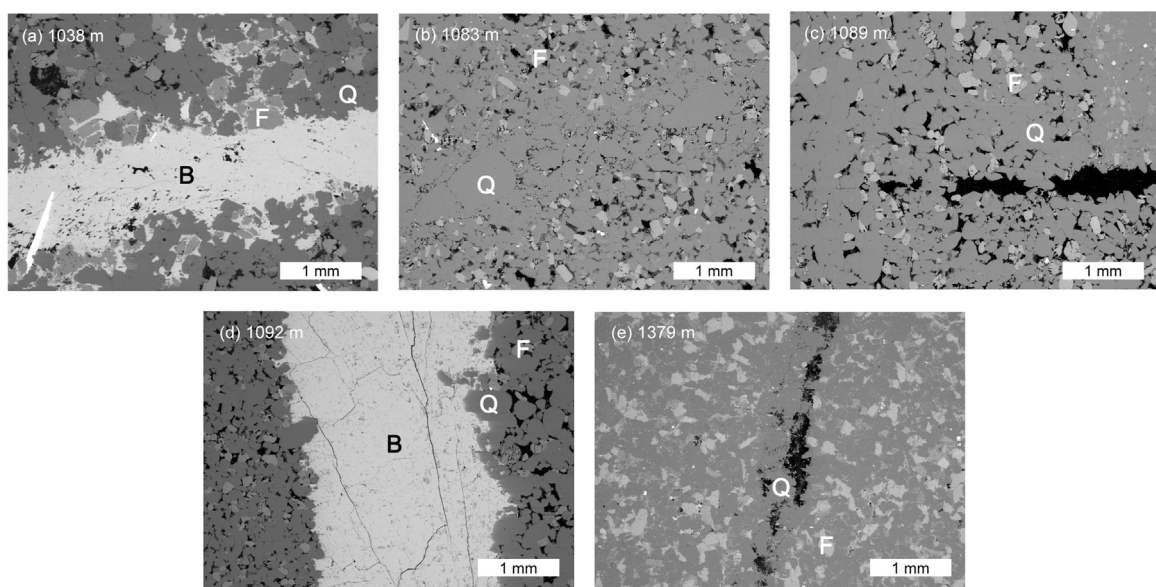


Fig. 4. SEM micrographs of thin sections from each core sample. SEM micrographs of thin sections of rock containing partially-sealed fractures. 'Q' and 'F' label the quartz and feldspar grains, respectively, and the porosity is black. (a) and (d) show thick fractures sealed by barite precipitation, labelled 'B'. At the bottom left of (a), is an elongated siderite crystal. The fractures in (b), (c) and (e) contain quartz and K-feldspar. Both (c) and (e) show only partial sealing.

gave an average fracture density of 0.83/m (Genter et al., 1997). These fractures are for the most part sub-vertical, and generally have a width of 0.1–3 mm. Their average width is about 2 mm however some rare fractures can be up to 5 cm wide (Vernoux et al., 1995). Fig. 1 is an example of the EPS1 Buntsandstein core containing a large fracture, roughly 1 cm in width, filled with precipitated

barite (BaSO_4). In terms of their spatial distribution, the fractures have a preferred orientation; the two major fracture sets strike N005° and N170°, dipping 70°W and 70°E respectively (Genter et al., 1997). Some of these fracture zones within the Buntsandstein have been shown to be permeable, through analysis of Soultz-sous-Forêts mud and well logging data (Vidal et al., 2015). In the same

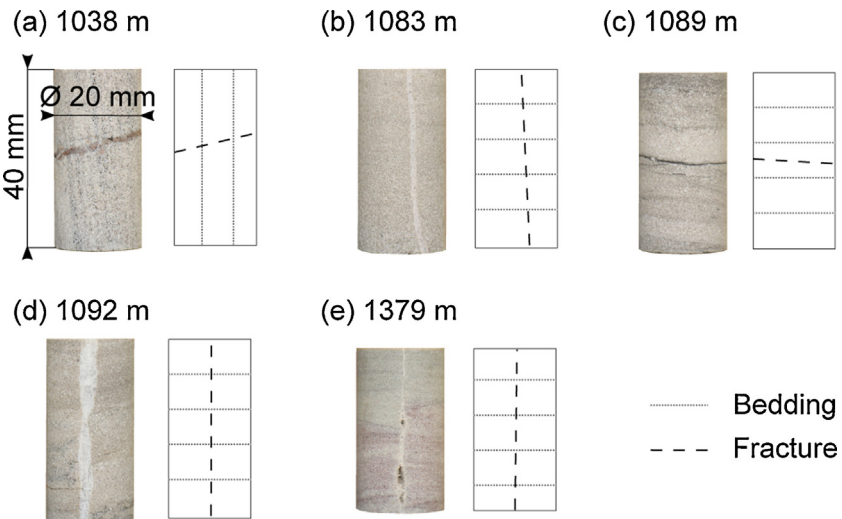


Fig. 5. Photographs of examples of the Buntsandstein samples from (a) 1038 m, (b) 1083 m, (c) 1089 m, (d) 1092 m, and (e) 1379 m depth. They contain fractures and bedding perpendicular or parallel to their axis, described by the drawing to their right. For a complete list of the 40 samples and their fracture and bedding orientations, see Table 2. These samples were subject to porosity and permeability measurements. Permeability was measured along their axes.

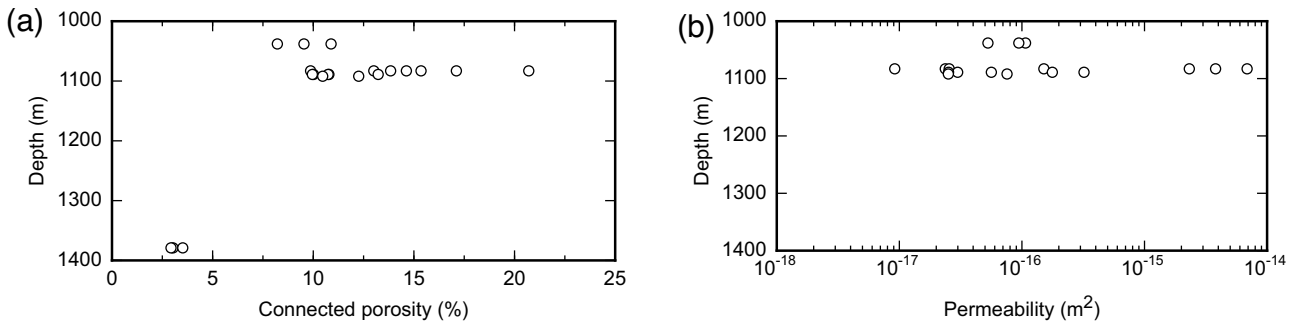


Fig. 6. (a) Porosity against depth for all of the intact samples (Table 2). At 1379 m depth, the variation of porosity between samples is very low. For the samples from shallower depths, however, the porosity is more variable, the 1038 m samples showing the smallest variation. (b) Permeability against depth for all of the intact, un-fractured samples from 1038 m, 1083 m, 1089 m, 1092 m depth (Table 2). Samples cored both parallel and perpendicular to bedding are represented. The 1379 m depth samples were too impermeable for our experimental setup ($<10^{-18} \text{ m}^2$). The permeability values of the 1038 m depth samples show the least variation. The values at other depths vary across several orders of magnitude.

study, the presence of secondary precipitated minerals within the fracture zones and an associated reduction in permeability is also discussed. Indeed, the importance of fracture sealing in a geothermal context has been highlighted by recent study by McNamara et al. (2016), who identify calcite sealing mechanisms in the Kawerau Geothermal Field, New Zealand. Fracture sealing is already known to occur in volcanic systems, which are highly dynamic with regards to temperature and fluid flow, and where mineral precipitation is expected to contribute to a decrease in permeability and create a barrier for fluids (Ball et al., 2015).

The above studies highlight the importance of the fractured Triassic Buntsandstein sandstone for regional fluid flow and temperature distribution, as well as the potential for mineral precipitation to influence fracture permeability. Hydraulic properties of the Buntsandstein host rock have been quantified through permeability measurements of the EPS1 core, including laboratory measurements (Sizun, 1995), and measurements using a TinyPerm II field permeameter (Haffen et al., 2013). Both studies find the permeability to vary with depth in the range of 10^{-16} – $5 \times 10^{-13} \text{ m}^2$. However, due to the anticipated importance of fracture sealing on regional permeability and permeability anisotropy, we provide in this study new laboratory porosity and permeability measurements on Buntsandstein core samples with and without partially-sealed and sealed fractures. We then look specifically at barite precip-

itation, which is abundant in fractures in the core samples, and model the crystal growth rate with temperature, providing a time scale for sealing. Finally, we discuss the geothermal implications for permeability anisotropy and its time dependency due to mineral precipitation.

2. Core description

For our study, we targeted borehole core from exploration well EPS1 well that best represents the variability of preserved fractures within the Buntsandstein (Fig. 2). Core was selected from sections where the fracture density is noticeably greater, in the Upper Buntsandstein (1038 m depth), the Middle Buntsandstein (1083 m, 1089 m, and 1092 m depth), and the Lower Buntsandstein (1379 m depth). Heterogeneity in grain size and cementation is macroscopically visible between the selected samples (Fig. 2). Bands of coarse grains (5–15 mm in width) are visible within the samples from 1083 m, 1089 m, and 1092 m depth. The sample from 1038 m depth shows less grain size heterogeneity. This is also the case at 1379 m depth where the core contains a red and green alternating coloration but a homogeneous grain size.

These core samples include sub-vertical fractures containing mineral precipitates. The fracture width ranges from 0.5 mm to 2 mm. These are representative of the preserved fractures in the

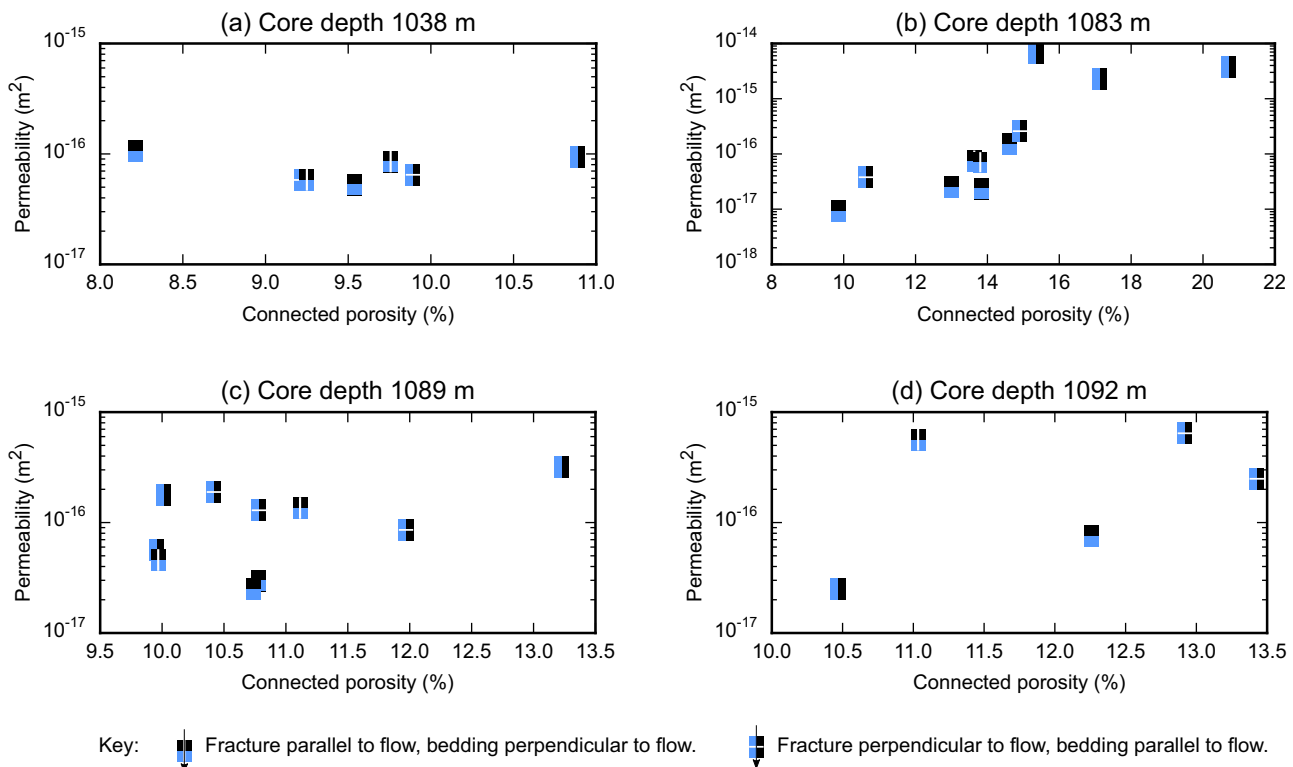


Fig. 7. Permeability against porosity for samples from (a) 1038 m, (b) 1083 m, (c) 1089 m, (d) 1092 m depth. The symbols show the orientation of the bedding and the fracture. Vertical white lines are fractures parallel to the sample axis i.e. the flow direction. Horizontal white lines are fractures perpendicular to flow. Similarly, two vertical blue and black stripes represent samples for which bedding is parallel to their axis and to fluid flow, two horizontal stripes represent bedding perpendicular to the flow direction. (For interpretation of the references to colour in this figure legend, the reader is referred to the web version of this article).

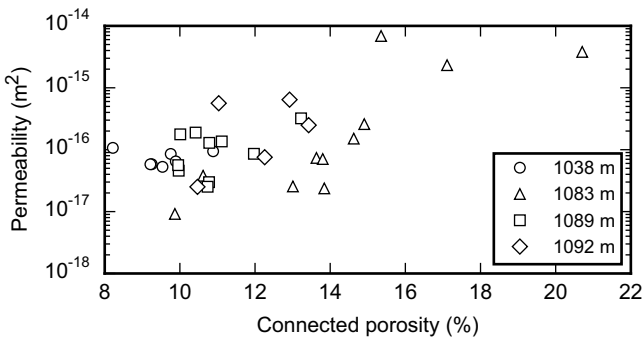


Fig. 8. Synopsis plot of permeability against porosity for all samples from 1038 m, 1083 m, 1089 m, 1092 m depth (Table 2). No distinction is made regarding the fracture or bedding orientations. The permeability of the Annweiler sandstone samples from 1379 m depth was too low to be measured with the apparatus used in this study ($<10^{-18} \text{ m}^2$).

EPS1 core (Vernoux et al., 1995) however, as mentioned above, some larger fractures are also present (Fig. 1). Slip along fractures can be observed, particularly in the case of the 1038 m, 1089 m, and 1379 m core samples where there is 5–10 mm of misalignment in bedding (Fig. 2). We see no misalignment inside the fracture filling at this scale.

3. Microstructural observations and host rock mineralogy

Thin sections were prepared from offcuts of the Buntsandstein containing the sealed fractures, one for each of the 5 depths of investigation. These were subject to scanning electron microscopy (SEM) to characterise the host rock (Fig. 3) and the fractures (Fig. 4).

3.1. Host rock

The host rock of the 1038 m depth sample (Fig. 3a) contains quartz and feldspar grains of around 0.5 mm in diameter and the feldspar is etched in some cases. At 1083 m depth (Fig. 3b), grains are finer, 0.1–0.2 mm in diameter. The thin section of the rock from 1089 m (Fig. 3c) contains bands of different grain sizes. Fine grains of 0.1–0.2 mm in diameter occupy most of the image while quartz grains of ~1 mm in diameter can be seen in the lower left hand corner of the image. At 1092 m depth (Fig. 3d), the grain size appears more homogeneous although there is still a band of larger grains and pores along the top half of the image. Finally, at 1379 m (Fig. 3e) depth we see grains of 0.1–0.3 mm in diameter and a reduced pore space compared to the previous samples.

X-Ray Diffraction (XRD) techniques were used to determine the bulk rock mineral composition (Table 1) at each depth. Two 1083 m samples were analysed due to the heterogeneity of the core at this depth. The samples were gently disaggregated using an agate mortar, resulting in 10–15 g of powdered material. For bulk rock mineral quantification, an aliquot was ground together with 10% ZnO as an internal standard for 8 min in 10 ml of isopropyl alcohol using a McCrone Micronising Mill with agate cylinder elements. The XRD analyses (2–70° 2θ) were performed on top-loaded powder mounts using a Philips PW 1800 X-ray diffractometer (CuKα, graphite monochromator, 10 mm automatic divergence slit, step-scan 0.02° 2θ increments per second, counting time 1 s per increment, 40 mA, 30 kV). The Rietveld program BGMINwin 1.8.6 was used for phase quantification. For clay mineralogical investigations, the sample was dispersed using an ultrasonic bath in deionized water. The <2 μm fraction was separated by sedimentation in Atterberg cylinders. The oriented clay mineral aggregates were prepared by sedimentation and air-drying of the aqueous sus-

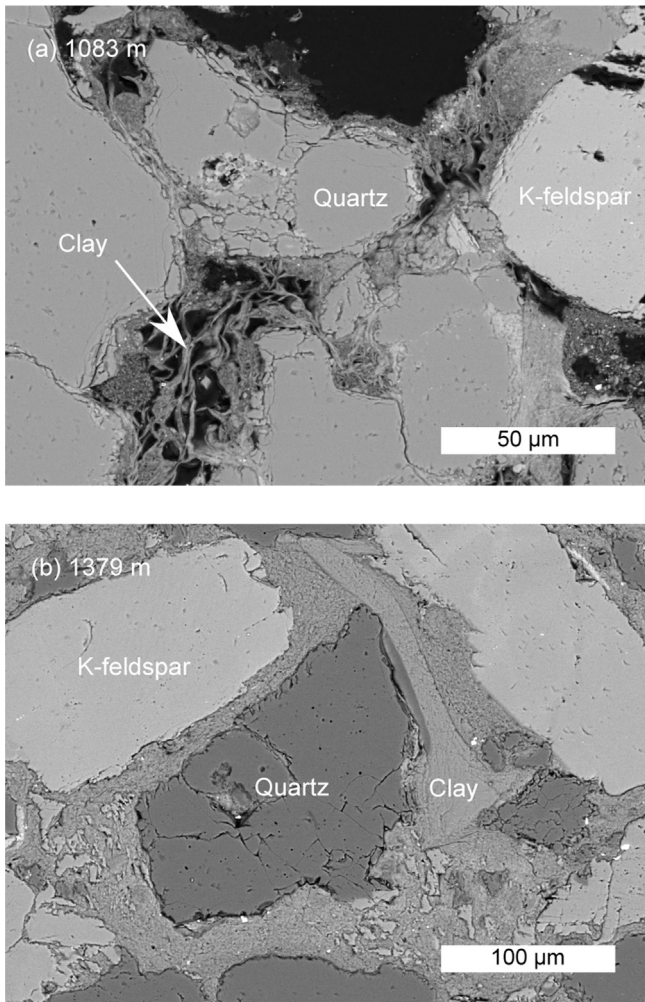


Fig. 9. SEM micrographs of thin sections of Buntsandstein EPS1 core samples from (a) 1083 m (Karlstal Beds) and (b) 1379 m depth (Annweiler sandstone). Pore-filling clays are visible in both images and in (b) they appear to occupy all the available pore space.

pension on glass slides. XRD scans ($2\text{--}30^\circ 2\theta$) were performed on both an air-dried and a glycolated (24 h in saturated glycol vapour at 80°C) mount.

The Buntsandstein samples contain quartz, K-feldspars (orthoclase and microcline), and an R3 interstratified illite-smectite with less than 5% expandable layers and possibly also discrete illite/mica. The 1379 m deep sample contains much more illitic material, (20 mass%) as compared to 1–3 mass% at shallower depths.

3.2. Fractures

Fig. 4 shows micrographs of the 5 thin sections containing sealed fractures. The fracture in the 1038 m depth sample (**Fig. 4a**) is 1 mm wide and is sealed with barite crystals. The 1083 m sample contains a 1 mm thick band composed of large quartz grains (**Fig. 4b**). The micrograph of the 1089 m core (**Fig. 4c**) shows a partially sealed fracture containing quartz and K-feldspar. The 1092 m sample (**Fig. 4d**) contains a large fracture (2 mm wide), completely sealed with barite. Finally, the 1379 m depth sample (**Fig. 4e**) hosts a variably sealed fracture containing clay and quartz grains.

4. Laboratory experiments

4.1. Sample preparation and experimental methods

Forty cylindrical samples (nominally 40 mm in length and 20 mm in diameter) were prepared from the borehole core such that they contained sealed or partially-sealed fractures either parallel or perpendicular to their axis. These samples were cored either parallel or perpendicular to bedding (the orientations are given in **Table 2**). We also prepared samples of the intact host rock, containing no fractures. Examples of the prepared samples are shown in **Fig. 5**. These samples were then subject to gas porosity measurements and gas permeability measurements. The connected porosity was calculated from the sample bulk volume measured using callipers and the rock matrix volume measured using a helium pycnometer (Micromeritics AccuPyc II 1340). Permeability measurements were made on jacketed samples using the steady state method, under a confining pressure of 1 MPa. Volumetric flow was measured using a gas flow meter for several pressure gradients across the sample. Two flow meters were used, one for high flow rates (i.e. high permeability samples) and one for low flow rates (i.e. low permeability samples). Darcy's law was used to calculate the permeability (applying the Klinkenberg or Forchheimer correction where necessary). The permeability range measurable with this setup is $10^{-18}\text{--}10^{-11}\text{ m}^2$.

4.2. Porosity and permeability of the intact rock samples

Connected porosity measurements of the intact Buntsandstein sandstone give values ranging from 2.9% to 20.7% (**Table 2**). These porosity measurements on the intact materials are shown in **Fig. 6a** as a function of depth. The samples from 1028 m depth have a relatively consistent porosity, ranging from 8.2% to 10.9%. The same is true for the values at 1089 m, which range from 10.0% to 13.2% and at 1089 m, which are between 10.5% and 13.2%. At 1083 m depth, the porosity is much more variable, 9.9%–20.7% which reflects the high variability of the core sample (**Fig. 2**). Finally, the 1379 m samples give very consistent values of around 3% porosity.

Permeability measurements of the Buntsandstein host rock yielded values ranging from 9.2×10^{-18} to $6.9 \times 10^{-15}\text{ m}^2$ (**Table 2**). The samples from 1379 m depth were too impermeable to be measured using our experimental setup ($<10^{-18}\text{ m}^2$). **Fig. 6b** is a synopsis plot containing all of the intact rock permeability data against depth, samples cored both parallel and perpendicular to bedding are presented. The permeability of the 1038 m core is less variable than the other samples (1083–1092 m depth), which span across several orders of magnitude.

4.3. Porosity and permeability of the fractured samples

Fig. 7 shows the permeability against the porosity values (**Table 2**) at each core depth plotted on separate graphs. The directions of the bedding and the fracture with regards to the flow direction is shown via the symbol representing each data point as explained in the figure caption. Note that the scales are different to better show the data. A synopsis plot, containing all of the porosity-permeability data, is shown in **Fig. 8**.

The porosity of samples extracted from 1038 m depth (**Fig. 7a**) varies between 8.2% and 10.9% and the permeability is in the range of $10^{-17}\text{--}10^{-16}\text{ m}^2$ for all samples, both show little variation, regardless of the presence and orientation of bedding and fractures.

In **Fig. 7b**, at 1083 m depth, we see more variability in the porosity (9.9–20.7%) and permeability ($9.2 \times 10^{-18}\text{--}6.9 \times 10^{-15}\text{ m}^2$). The permeability of the intact (fracture free) samples is around 2 orders of magnitude higher for samples cored parallel to the bedding. The permeability of these samples cored parallel to the bedding is how-

Table 2

Porosity and permeability measurements of all 40 Buntsandstein samples. For the permeability tests, the fluid flow direction with regards to bedding and fracture orientation is given.

Measured depth (m)	Lithostratigraphy	Connected porosity (%)	Permeability (m^2)	Bedding vs. flow direction	Fracture vs. flow direction	Approximate fracture aperture (mm)
1038	Upper Buntsandstein – Intermediate Beds	9.3	5.8×10^{-17}	perpendicular	parallel	1–2
1038	"	9.8	8.5×10^{-17}	perpendicular	parallel	1
1038	"	9.5	5.3×10^{-17}	perpendicular	intact	–
1038	"	8.2	1.1×10^{-16}	perpendicular	intact	–
1038	"	9.9	6.5×10^{-17}	parallel	perpendicular	1–2
1038	"	9.2	5.8×10^{-17}	parallel	perpendicular	1–2.5
1038	"	10.9	9.4×10^{-17}	parallel	intact	–
1083	Middle Buntsandstein – Karlstal Beds	9.9	9.2×10^{-18}	perpendicular	intact	–
1083	"	14.6	1.5×10^{-16}	perpendicular	intact	–
1083	"	17.1	2.3×10^{-15}	parallel	intact	–
1083	"	20.7	3.8×10^{-15}	parallel	intact	–
1083	"	13.8	2.4×10^{-17}	perpendicular	intact	–
1083	"	13.6	7.4×10^{-17}	perpendicular	parallel	1–2
1083	"	13.0	2.5×10^{-17}	perpendicular	intact	–
1083	"	13.8	7.1×10^{-17}	perpendicular	parallel	1–1.5
1083	"	15.4	6.9×10^{-15}	parallel	intact	–
1083	"	14.9	2.6×10^{-16}	parallel	perpendicular	1–2
1083	"	10.6	3.8×10^{-17}	parallel	perpendicular	1–2
1089	Middle Buntsandstein – Karlstal Beds	10.4	1.9×10^{-16}	parallel	perpendicular	0.5–1
1089	"	10.0	1.8×10^{-16}	parallel	intact	–
1089	"	10.0	4.6×10^{-17}	perpendicular	parallel	0.5–1
1089	"	11.1	1.4×10^{-16}	perpendicular	parallel	0.5–1.5
1089	"	10.8	3.0×10^{-17}	perpendicular	intact	–
1089	"	10.7	2.5×10^{-17}	perpendicular	intact	–
1089	"	12.0	8.6×10^{-17}	parallel	perpendicular	0.5–1.5
1089	"	10.8	1.3×10^{-16}	parallel	perpendicular	0.5–1.5
1089	"	10.0	5.6×10^{-17}	parallel	intact	–
1089	"	13.2	3.2×10^{-16}	parallel	intact	–
1092	Middle Buntsandstein – Karlstal Beds	11.0	5.6×10^{-16}	perpendicular	parallel	2–4
1092	"	12.3	7.6×10^{-17}	perpendicular	intact	–
1092	"	13.4	2.5×10^{-16}	parallel	perpendicular	2–4.5
1092	"	10.5	2.5×10^{-17}	parallel	intact	–
1092	"	12.9	6.4×10^{-16}	parallel	perpendicular	0.5–1
1379	Lower Buntsandstein – Annweiler Sandstone	3.6	$<10^{-18}$	perpendicular	parallel	0.5–1
1379	"	3.7	$<10^{-18}$	perpendicular	parallel	0.5–2
1379	"	3.0	$<10^{-18}$	perpendicular	intact	–
1379	"	2.9	$<10^{-18}$	perpendicular	intact	–
1379	"	3.7	$<10^{-18}$	parallel	perpendicular	0.5–1.5
1379	"	3.5	$<10^{-18}$	parallel	intact	–

ever lower for those containing a sealed fracture perpendicular to the flow direction. The permeability of samples containing a sealed fracture parallel to flow are roughly the same permeability as the host rock.

The samples from 1089 m depth (Fig. 7c) show a lower variation in porosity (10.0–13.2%) whereas the permeability can vary by more than an order of magnitude. Generally, the permeability parallel to the bedding is greater, as is the case at 1083 m depth. It is difficult to pick out a trend regarding the flow vs. fracture direction.

The porosity of the 1092 m samples ranges from 10.5 to 13.4% and the permeability from 2.5×10^{-17} to $6.4 \times 10^{-16} \text{ m}^2$ (Fig. 7d). The permeability values are roughly an order of magnitude higher for samples containing a fracture (regardless of the fracture orientation).

5. Discussion

5.1. Permeability of the buntsandstein

Our permeability measurements yield values in the range of 9.2×10^{-18} – $6.9 \times 10^{-15} \text{ m}^2$ (Table 2) for the measurable samples (i.e. all but the 1379 m depth core, which has a significantly lower permeability). We see a general trend of increasing permeability with porosity (Fig. 8). Previous studies on porous sandstones with a connected porosity in the range of 4% to 35% reported permeability values in the range of 10^{-16} m^2 – $2 \times 10^{-12} \text{ m}^2$ (Bourbié and Zinszner, 1985; David et al., 1994; Zhu and Wong, 1997; Vajdová et al., 2004; Baud et al., 2012). Considering the connected porosities of these samples, 8.2–20.7%, this permeability range could therefore be considered low for sandstone. As mentioned above, the permeability of the samples from 1379 m depth was even not measurable using our apparatus ($<10^{-18} \text{ m}^2$). A likely explanation for this is the prevalence of clay at all depths. SEM images, for exam-

ple, show an abundance of pore-filling clays (examples shown in Fig. 9). This is especially the case for the Annweiler sandstone at 1379 m depth, where the pore space is drastically diminished (Fig. 9b) and clay is also visible in the fracture itself (Fig. 4e) (see also Vernoux et al., 1995). This was subsequently confirmed by XRD results (Table 1) where Illite-smectite is omnipresent, notably at 1379 m depth where it occupies 20 mass% of the bulk rock. These clay minerals which appear to block the pore throats could explain the low permeability of our samples (Table 2, Fig. 8). Furthermore, our permeability measurements were made using nitrogen gas as the permeant and due to the clay content in some samples, the water permeability could well be lower (Davy et al., 2007; Faulkner and Rutter, 2000; Tanikawa and Shimamoto, 2006; Tanikawa and Shimamoto, 2009). A previous study of the EPS1 Buntsandstein core measured permeability of the host rock with depth using a TinyPerm II field permeameter (which has a working range of 10^{-16} – 10^{-11} m^2) and gave values from 10^{-16} m^2 to $5 \times 10^{-13} \text{ m}^2$ (Haffen et al., 2013). Our laboratory measurements of some samples of the Middle Buntsandstein host rock yield values within this range (Fig. 6b), however all other samples were found to be less permeable, highlighting the limitations of the TinyPerm for certain units of the Buntsandstein.

We highlight that samples are 40 mm in length and 20 mm in diameter and cannot therefore take into account reservoir-scale heterogeneities such as meso and macro scale fractures. They do, on the other hand, contain fractures with apertures representative of those observed in well EPS1 (Table 2; Vernoux et al., 1995).

5.2. Permeability anisotropy of the buntsandstein

For all samples, our XRD results show that the precipitated hydrothermal minerals seen in the fractures (Figs. 2 and 4) are not present in the bulk rock (Table 1). This suggests that these fractures were once conduits for geothermal brines. However, through mineral precipitation, their permeability has likely decreased. As the fractures have a preferred orientation, striking N005° and N170° and dipping 70°W and 70°E respectively (Genter et al., 1997) the degree of permeability anisotropy within this unit may have therefore diminished over time if the sealed fractures exist on a reservoir length scale. The lack of precipitated hydrothermal minerals in the host rock of these materials suggest that the fluids utilise other channels through the fracture or switched to adjacent open or partially-sealed fractures. An extreme scenario would be where these large vertical fractures become completely sealed by precipitates and compartmentalise large scale fluid flow.

We observe an anisotropy due to bedding (see in particular Figs. 7b and c) and that sealed or partially sealed fractures could serve to homogenise the permeability of certain layer within the Buntsandstein (Fig. 10). For example, the high permeability parallel to bedding in the intact 1083 m depth Karlstal Beds samples (Fig. 7b) is reduced to the lower permeability of the samples cored perpendicular to bedding in the presence of sealed fractures. These sealed fractures are effectively cancelling the anisotropy due to bedding.

Both at the core scale and in the SEM images, the extent of fracture sealing within the Buntsandstein unit is visibly variable. Indeed, (Vernoux et al., 1995), give a ratio of the free aperture per total fracture aperture of 0.2 for the entire population of fractures in the Buntsandstein. This is reflected in the permeability measurements (Fig. 7), where partially sealed fractures may still act as conduits for flow (see also Neuville et al., 2012a; Neuville et al., 2012b). Within our sample set, the extent of sealing seems to depend on the nature of the precipitate and barite precipitation seems to be the most efficient at sealing large fractures (e.g. Fig. 1), as well as one of the most abundant in the core. For this reason, we

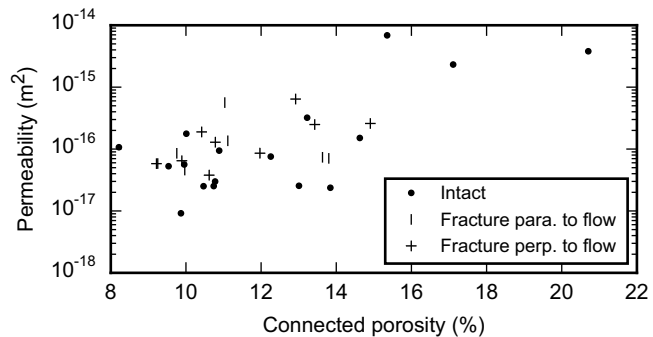


Fig. 10. Synopsis plot of permeability against porosity for all samples from 1038 m, 1083 m, 1089 m, 1092 m depth (Table 2). Data points are grouped according to the presence and orientation of fractures with regards to flow (parallel or perpendicular). The permeability of the Annweiler sandstone samples from 1379 m depth was too low to be measured with the apparatus used in this study ($<10^{-18} \text{ m}^2$).

chose to model the growth rate of barite crystals in a geothermal context to quantify the time required for fracture sealing.

5.3. A time scale for fracture sealing

Barite (BaSO_4) scaling is commonly observed in hydrocarbon reservoirs where highly concentrated brines are extracted from oil wells (Templeton, 1960). The same is true at the Soultz-sous-Forêts geothermal site, where it is abundant in the well core (Vernoux et al., 1995). Furthermore, barite is the most common precipitate in Soultz-sous-Forêts scaling and has been observed in pipes at the surface installations (Scheiber et al., 2013). Moreover, due to the extremely low solubility of barite, it requires mechanical removal (Christy and Putnis, 1993) which halts production and is both expensive and time consuming. Because of these risks, it is important to understand how quickly barite could precipitate in a geothermal context.

Strictly speaking, overall precipitation rate laws for any mineral should account for both the nucleation and growth steps (e.g. Fritz and Noguera, 2009). However, for most minerals, critical data that are required to model the nucleation step are currently missing (e.g. interfacial energy, see Fernandez-Martinez et al., 2013), such that studies aimed at modelling the precipitation rate of secondary phases often focus on the growth step, starting with an ad hoc precursor surface (see Dava et al., 2009 and references therein). A similar strategy was applied here, starting from nuclei with a size corresponding to that of a primitive cell of barite. Such a conservative choice ensures that barite precipitation rate is not artificially overestimated. The model for the crystal growth rate of barite relies on the rate Eq. (1), which gives the precipitation rate of barite R_T ($\text{mol}/\text{m}^2/\text{s}$) for a given temperature T . This is a second order rate law, characteristic of spiral growth (Christy and Putnis, 1993) and is a function of the rate constant k_T ($\text{mol}/\text{m}^2/\text{s}$), and Ω_T , which is the reaction quotient divided by the equilibrium constant for barite precipitation.

$$R_T = k_T (\Omega_T - 1)^2 \quad (1)$$

An Arrhenius law (2) relates the rate constant k_T to temperature. The pre-exponential factor k_0 ($\text{mol}/\text{m}^2/\text{s}$) and the activation energy E_a (J) were calculated using data from Christy and Putnis, 1993. R_m is the universal gas constant and T (K) is the temperature of the solution.

$$k_T = k_0 \exp \left(-\frac{E_a}{R_m T} \right) \quad (2)$$

The values of Ω_T were calculated using the CHESS (Chemical Equilibrium of Species and Surfaces) program (van der Lee and De Windt, 2002), which models the equilibrium state of complex

Table 3

Analytical fluid composition data from well GPK-1 (taken from Sanjuan et al., 2010).

Well	GPK1-KD006
Depth (m)	1845
pH	5.02
Na (g/L)	28
K (g/L)	3.28
Ca (g/L)	7.3
Cl (g/L)	58.1
SO ₄ (mg/L)	220
Ba (mg/L)	12.5

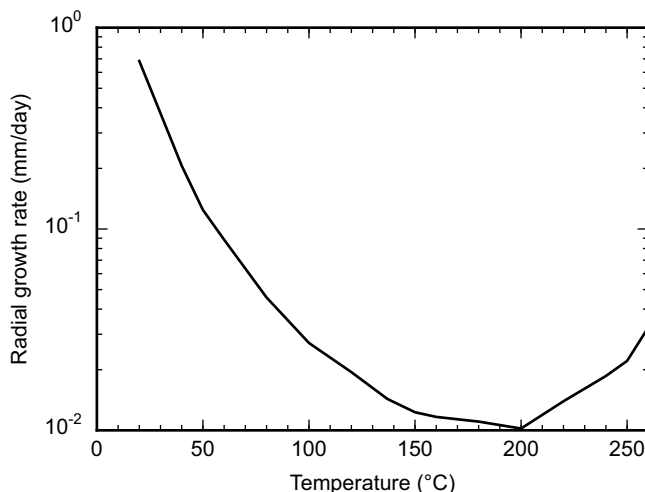


Fig. 11. The modelled barite crystal radial growth rate against temperature as calculated from Christy and Putnis, 1993. The growth rate is lowest at temperatures of around 200 °C and increases dramatically with decreasing temperature. The growth rate increases with temperature above 200 °C.

aquatic systems. The chemical composition of the Soultz-sous-Forêts brine was the input for the CHESS model (Table 3, from Sanjuan et al., 2010). These data are the closest available (from well GPK1, 500 m away) to our Buntsandstein EPS1 core and are from a similar depth (1845 m). The chemical composition is sufficiently homogeneous to be assumed constant with depth (Sanjuan et al., 2010). We consider only the effect of temperature on barite precipitation, ignoring any variation in fluid composition. For hydrocarbon or geothermal reservoirs, the injection fluid (often seawater) can differ to the fluid in the reservoir. The fluid mixing of injected salty seawater, which has a high sulphate content, with in-situ barium rich hydro-geothermal fluid can encourage barite scaling (Sorbie and Mackay, 2000). In our case, sulphate concentrations are already high and therefore our model does not take fluid mixing into account.

From the precipitation rate R_T at different temperatures (1), and assuming a spherical barite crystal, we can infer the radial growth rate (3). Here ρ and M are respectively the density and the molar mass of barite.

$$\left[\frac{dr}{dt} \right]_T = \frac{3MR_T}{\rho} \quad (3)$$

Fig. 11 shows the modelled radial growth rate of a barite crystal against temperature. Up to 200 °C, the growth rate decreases dramatically with temperature. These results, which may seem intriguing because k_T is an intrinsic function of T , actually underline the critical role of the temperature dependence of barite solubility. They are further supported by a study by Templeton, 1960, who finds an increase in the solubility of barite with temperature for solutions within the range of 25–95 °C. Above 200 °C, the trend inverses and we see an increase of the growth rate with tempera-

ture. We note that barite solubility has been shown to increase with pressure (Blount, 1977) so that the depressurisation of geothermal brines will also encourage precipitation.

5.4. Geothermal implications

As discussed above, the permeability of the host Buntsandstein is reduced due to pore-filling clays (Fig. 9). When it comes to modelling fluid flow, the permeability of the Buntsandstein plays an important role at Soultz-sous-Forêts. Indeed, assigning low permeability values ($<10^{-14} \text{ m}^2$) to the Triassic sediments has been shown to inhibit the formation of fluid convection cells (Magenet et al., 2014). Although some layers may be permeable ($>10^{-15} \text{ m}^2$), the presence of low permeability layers would suggest that for large scale convection to occur within the Buntsandstein as a whole, open or partially sealed fractures must be available to facilitate fluid flow.

The precipitation rate of barite increases dramatically with decreasing temperature (Fig. 11). At the Soultz-sous-Forêts geothermal site, sulphate and sulphide scaling is particularly visible in the cold part of the surface installations where water is cooled from 160 °C to 60 °C, but scaling can even appear in the injection well (Scheiber et al., 2013). During production tests in November 2008 at Soultz-sous-Forêts, geothermal brine was extracted from the reservoir at around 155 °C and re-injected at 50 °C (Genter et al., 2009). The modelled crystal growth rate (Fig. 11) would suggest that given the same composition, barite crystals will form 10 times faster from the cooler fluid (from 0.01 mm/day to 0.1 mm/day in radial growth). These calculated rates are consistent with observations at the surface installations where, in 2011, between cleaning the heat exchanger in March and opening it in September to sample scalings, a barite-celestine solid solution (Ba,Sr)SO₄ formed platelets of a few millimetres in thickness (Nitschke et al., 2014).

At Soultz-sous-Forêts, temperatures can reach 200 °C at 5 km depth (Genter et al., 2010) and if the saturated geothermal brine were to circulate upwards and cool, it would encourage a faster precipitation. This would be especially true if deep geothermal fluids were to reach 1 km depth, above which the thermal gradient is much higher than the 5 °C/km measured between 1.5 and 3.5 km depth. Within the Buntsandstein, the fluid temperature is around 130 °C and at this temperature, the model gives a radial growth rate of barite crystals to be around 1.5×10^{-2} mm/day. To better understand the typical radius of a barite crystal, we used polarised light microscopy to distinguish the crystal orientation of individual barite crystals in the thin section from 1092 m depth (Fig. 4d). We found they each span roughly 1 mm across the fracture aperture, i.e. for the spherical model they have an equivalent radius of around 0.5 mm. In this case, at a radial growth rate of 1.5×10^{-2} mm/day, a 2 mm wide fracture (the average fracture aperture of the Buntsandstein, Table 2; Vernoux et al., 1995) could seal in around 1 month, well within the 20–50 year lifetime of a producing geothermal site. We note that this simple model does not take into account the spatial variability of the precipitation rate due to the channeling of flow (Méheust and Schmittbuhl, 2001). Despite these short sealing time scales, open and partially sealed fractures are still observed in the Buntsandstein, and this could be explained by slip along fractures, keeping permeable pathways open.

Since fractures influence fluid flow in the reservoir, as well as ensuring its hydraulic connection to the injection well, mineral precipitation could therefore have a large impact on geothermal production. The precipitation rate is a function of the temperature and composition of the injected fluids which could be manipulated if required. The addition of chemical precipitation inhibitors to the injection fluid is also an efficient, but expensive, solution (e.g. Scheiber et al., 2013).

6. Conclusion

Generally speaking, open fractures are thought to affect the permeability and permeability anisotropy of geothermal reservoirs. In particular, the Triassic Buntsandstein sandstone (1–1.4 km depth), an important unit for regional fluid flow at Soultz-sous-Forêts, exhibits a dense fracture network. Microstructural observations of selected Buntsandstein core samples show how these fractures are variably sealed by precipitated minerals and therefore their influence on fluid flow is less predictable. We quantified, through new porosity and permeability measurements, the hydraulic properties of the Buntsandstein. As a result of pore-filling clays, the values of permeability of the host rock were lower than we expected based on porosity and permeability data on similarly porous sandstones. We found that the presence of low permeability sealed fractures can homogenise the permeability anisotropy (for example due to bedding), although we highlight that at the reservoir scale, fluids may find new vertical pathways through remaining open or partially-sealed fractures. These results highlight the importance of mineral precipitation at a geothermal site, as both well injectivity and regional fluid flow depend on a reliable network of permeable fractures. To look at the time scale for sealing, we specifically targeted the precipitation of barite, seen at Soultz-sous-Forêts and in many other hydro-geothermal contexts worldwide. Our model takes into account the Soultz-sous-Forêts geothermal fluid composition and gives the precipitation rate of barite as a function of temperature, showing it to decrease as the geothermal fluid cools. Between the temperatures at the extraction well (~150 °C) and the re-injection well (~50 °C), the modelled crystal growth rate increases by an order of magnitude. Within the Buntsandstein, at around 130 °C, the radial growth rate of barite crystals is predicted to be around 10⁻² mm/day meaning that the permeability of a geothermal reservoir around the injection well could vary greatly over the course of production.

Acknowledgements

The authors would like to thank GEIE Exploitation Minière de Chaleur for providing the Soultz core samples and relevant information; Bertrand Renaudié for sample preparation; Gilles Morvan for his SEM assistance; and Jamie Farquharson and Alex Kushnir for the development and maintenance of the permeameter. The authors acknowledge the support of the French Agence Nationale de la Recherche (ANR), under grant ANR-ANR-15-CE06-0014-01 (project CANTARE). This work has been published under the framework of LABEX grant ANR-11-LABX-0050_G-EAU-THERMIE-PROFONDE and therefore benefits from state funding managed by the Agence National de la Recherche (ANR) as part of the “Investissements d’avenir” program.

References

- Ball, J.L., Stauffer, P.H., Calder, E.S., Valentine, G.A., 2015. The hydrothermal alteration of cooling lava domes. *Bull. Volcanol.* 77, <http://dx.doi.org/10.1007/s00445-015-0986-z>.
- Baria, R., Baumgärtner, J., Gérard, A., Jung, R., Garnish, J., 1999. European HDR research programme at soultz-sous-Forêts (France) 1987–1996. *Geothermics* 28, 655–669, [http://dx.doi.org/10.1016/s0375-6505\(99\)00036-x](http://dx.doi.org/10.1016/s0375-6505(99)00036-x).
- Baud, P., Meredith, P., Townend, E., 2012. Permeability evolution during triaxial compaction of an anisotropic porous sandstone. *J. Geophys. Res. Solid Earth* 117, <http://dx.doi.org/10.1029/2012JB009176>.
- Blount, C.W., 1977. Barite solubilities and thermodynamic quantities up to 300 degrees C and 1400 bars. *Am. Mineral.* 62, 942–957.
- Bourbié, T., Zinszner, B., 1985. Hydraulic and acoustic properties as a function of porosity in Fontainebleau Sandstone. *J. Geophys. Res. Solid Earth* 90, 11524–11532, <http://dx.doi.org/10.1029/JB090iB13p11524>.
- Christy, A.G., Putnis, A., 1993. The kinetics of barite dissolution and precipitation in water and sodium chloride brines at 44–85 °C. *Geochim. Cosmochim. Acta* 57, 2161–2168, [http://dx.doi.org/10.1016/0016-7037\(93\)90557-D](http://dx.doi.org/10.1016/0016-7037(93)90557-D).
- Daval, D., Martinez, I., Corvisier, J., Findling, N., Goffé, B., Guyot, F., 2009. Carbonation of Ca-bearing silicates, the case of wollastonite: experimental investigations and kinetic modeling. *Chem. Geol.* 265, 63–78, <http://dx.doi.org/10.1016/j.chemgeo.2009.01.022>.
- David, C., Wong, T.-F., Zhu, W., Zhang, J., 1994. Laboratory measurement of compaction-induced permeability change in porous rocks: implications for the generation and maintenance of pore pressure excess in the crust. *Pure Appl. Geophys.* 143, 425–456, <http://dx.doi.org/10.1007/BF00874337>.
- Davy, C.A., Skoczyłas, F., Barnichon, J.-D., Lebon, P., 2007. Permeability of macro-cracked argillite under confinement: gas and water testing. *Phys. Chem. Earth Parts ABC* 32, 667–680, <http://dx.doi.org/10.1016/j.pce.2006.02.055>.
- Dezayes, C., Genter, A., Valley, B., 2010. Structure of the low permeable naturally fractured geothermal reservoir at Soultz. *C. R. Geosci.* 342, 517–530, <http://dx.doi.org/10.1016/j.crte.2009.10.002>.
- Faulkner, D.R., Rutter, E.H., 2000. Comparisons of water and argon permeability in natural clay-bearing fault gouge under high pressure at 20 °C. *J. Geophys. Res.* 105, 415–416, <http://dx.doi.org/10.1029/2000jb900134>.
- Fernandez-Martinez, A., Hu, Y., Lee, B., Jun, Y.-S., Waychunas, G.A., 2013. In situ determination of interfacial energies between heterogeneously nucleated CaCO₃ and quartz substrates: thermodynamics of CO₂ mineral trapping. *Environ. Sci. Technol.* 47, 102–109, <http://dx.doi.org/10.1021/es3014826>.
- Fritz, B., Noguera, C., 2009. Mineral precipitation kinetics. *Rev. Mineral. Geochem.* 70, 371–410, <http://dx.doi.org/10.2138/rmg.2009.70.8>.
- Gérard, A., Genter, A., Kohl, T., Lutz, P., Rose, P., Rummel, F., 2006. The deep EGS (Enhanced geothermal system) project at soultz-sous-Forêts (Alsace, France). *Geothermics* 35, 473–483, <http://dx.doi.org/10.1016/j.geothermics.2006.12.001>.
- Genter, A., Traineau, H., 1996. Analysis of macroscopic fractures in granite in the HDR geothermal well EPS-1, Soultz-sous-Forêts, France. *J. Volcanol. Geotherm. Res.* 72, 121–141, [http://dx.doi.org/10.1016/0377-0273\(95\)00070-4](http://dx.doi.org/10.1016/0377-0273(95)00070-4).
- Genter, A., Castaing, C., Dezayes, C., Tenzer, H., Traineau, H., Villemot, T., 1997. Comparative analysis of direct (core) and indirect (borehole imaging tools) collection of fracture data in the Hot Dry Rock Soultz reservoir (France). *J. Geophys. Res.* 102, 15419, <http://dx.doi.org/10.1029/97JB00626>.
- Genter, A., Fritsch, D., Cuenot, N., Baumgärtner, J., Graff, J.-J., 2009. Overview of the current activities of the European EGS Soultz project: from exploration to electricity production. In: *Proceedings, 34th Workshop on Geothermal Reservoir Engineering*. Standford University, Standford, California USA, pp. 9–11.
- Genter, A., Evans, K., Cuenot, N., Fritsch, D., Sanjuan, B., 2010. Contribution of the exploration of deep crystalline fractured reservoir of Soultz to the knowledge of enhanced geothermal systems (EGS). *C. R. Geosci.* 342, 502–516, <http://dx.doi.org/10.1016/j.crte.2010.01.006>.
- Genter, A., 2010. Contribution of the exploration of deep crystalline fractured reservoir of Soultz to the knowledge of enhanced geothermal systems (EGS). *C. R. Geosci.* 342, 502–516, <http://dx.doi.org/10.1016/j.crte.2010.01.006>.
- Grant, M.A., Bixley, P.F., 2011. *Geothermal Reservoir Engineering*, 2nd ed. Academic Press, Burlington, MA.
- Guillou-Frottier, L., Carré, C., Bourgine, B., Bouchot, V., Genter, A., 2013. Structure of hydrothermal convection in the Upper Rhine Graben as inferred from corrected temperature data and basin-scale numerical models. *J. Volcanol. Geotherm. Res.* 256, 29–49, <http://dx.doi.org/10.1016/j.jvolgeores.2013.02.008>.
- Haffen, S., Géraud, Y., Diraison, M., Dezayes, C., 2013. Determination of fluid-flow zones in a geothermal sandstone reservoir using thermal conductivity and temperature logs. *Geothermics* 46, 32–41, <http://dx.doi.org/10.1016/j.geothermics.2012.11.001>.
- Kappelmeyer, O., Gérard, A., 1989. The european geothermal project at soultz-sous-Forêts. In: Ramberg, I.B., Neu-Mann, E.R. (Eds.), *The European Geothermal Update: Proceedings of the Fourth International Seminar on the Results of EC Geothermal Energy Research and Demonstration*, 285–554.
- Ledésert, B., Dubois, J., Genter, A., Meunier, A., 1993. Fractal analysis of fractures applied to Soultz-sous-Forêts hot dry rock geothermal program. *J. Volcanol. Geotherm. Res.* 57, 1–17, [http://dx.doi.org/10.1016/0377-0273\(93\)90028-P](http://dx.doi.org/10.1016/0377-0273(93)90028-P).
- Méheust, Y., Schmittbuhl, J., 2001. Geometrical heterogeneities and permeability anisotropy of rough fractures. *J. Geophys. Res. Solid Earth* 106, 2089–2102, <http://dx.doi.org/10.1029/2000JB000306>.
- Magnenet, V., Fond, C., Genter, A., Schmittbuhl, J., 2014. Two-dimensional THM modelling of the large scale natural hydrothermal circulation at Soultz-sous-Forêts. *Geotherm. Energy* 2, <http://dx.doi.org/10.1186/s40517-014-0017-x>.
- McNamara, D.D., Lister, A., Prior, D.J., 2016. Calcite sealing in a fractured geothermal reservoir: insights from combined EBSD and chemistry mapping. *J. Volcanol. Geotherm. Res.* 323, 38–52, <http://dx.doi.org/10.1016/j.jvolgeores.2016.04.042>.
- Neuville, A., Toussaint, R., Schmittbuhl, J., 2012a. Fracture aperture reconstruction and determination of hydrological properties: a case study at Draix (French Alps). *Hydrol. Processes* 26, 2095–2105, <http://dx.doi.org/10.1002/hyp.7985>.
- Neuville, A., Toussaint, R., Schmittbuhl, J., Koehn, D., Schwarz, J.-O., 2012b. Characterization of major discontinuities from borehole cores of the black consolidated marl formation of Draix (French Alps). *Hydrol. Processes* 26, 2085–2094, <http://dx.doi.org/10.1002/hyp.7984>.
- Nitschke, F., Scheiber, J., Kramar, U., Neumann, T., 2014. Formation of alternating layered Ba-Sr-sulfate and Pb-sulfide scaling in the geothermal plant of Soultz-sous-Forêts, Neues Jahrb für Mineral. –Abh. J. Mineral. Geochem. 191, 145–156, <http://dx.doi.org/10.1127/0077-7757/2014/0253>.

- Pribnow, D., Clauser, C., 2000. Heat and fluid flow at the Soultz hot dry rock system in the Rhine Graben. In: World Geothermal Congress, Kyushu-Tohoku Japan, pp. 3835–3840.
- Sanjuan, B., Millot, R., Dezayes, C., Brach, M., 2010. Main characteristics of the deep geothermal brine (5 km) at Soultz-sous-Forêts (France) determined using geochemical and tracer test data. *C. R. Geosci.* 342, 546–559, <http://dx.doi.org/10.1016/j.crte.2009.10.009>.
- Sausse, J., Dezayes, C., Dorbath, L., Genter, A., Place, J., 2010. 3D model of fracture zones at Soultz-sous-Forêts based on geological data, image logs, induced microseismicity and vertical seismic profiles. *C. R. Geosci.* 342, 531–545, <http://dx.doi.org/10.1016/j.crte.2010.01.011> (Vers l'exploitation des ressources géothermiques profondes des systèmes hydrothermaux convectifs en milieux naturellement fracturés. On the way to the exploitation of deep geothermal resources in naturally fractured environments).
- Scheiber, J., Seibt, A., Birner, J., Genter, A., Moeckes, W., 2013. Application of a scaling inhibitor system at the geothermal power plant in soultz-sous-Forêts: laboratory and on-Site studies. Proceedings European Geothermal Congress.
- Sizun, J.-P., (1995). Modification des structures de porosité de grès lors de transformations petrographiques dans la diagenèse et l'hydrothermalisme. Université Louis Pasteur, Strasbourg, France, Institut de Géologie Strasbourg.
- Sorbie, K.S., Mackay, E.J., 2000. Mixing of injected, connate and aquifer brines in waterflooding and its relevance to oilfield scaling. *J. Pet. Sci. Eng.* 27, 85–106, [http://dx.doi.org/10.1016/S0920-4105\(00\)00050-4](http://dx.doi.org/10.1016/S0920-4105(00)00050-4).
- Surma, F., Géraud, Y., 2003. Porosity and thermal conductivity of the soultz-sous-Forêts granite. In: Kümpel, H.-J. (Ed.), Thermo-Hydro-Mechanical Coupling in Fractured Rock, Pageoph Topical Volumes. Birkhäuser, Basel, pp. 1125–1136.
- Tanikawa, W., Shimamoto, T., 2006. Klinkenberg effect for gas permeability and its comparison to water permeability for porous sedimentary rocks. *Hydrol. Earth Syst. Sci. Discuss.* 3, 1315–1338.
- Tanikawa, W., Shimamoto, T., 2009. Comparison of Klinkenberg-corrected gas permeability and water permeability in sedimentary rocks. *Int. J. Rock Mech. Min. Sci.* 46, 229–238, <http://dx.doi.org/10.1016/j.ijrmms.2008.03.004>.
- Templeton, C.C., 1960. Solubility of barium sulfate in sodium chloride solutions from 25° to 95° C. *J. Chem. Eng. Data* 5, 514–516, <http://dx.doi.org/10.1021/je60008a028>.
- Vajdova, V., Baud, P., Wong, T., 2004. Permeability evolution during localized deformation in Bentheim sandstone. *J. Geophys. Res. Solid Earth* 109, <http://dx.doi.org/10.1029/2003JB002942>.
- Van der Lee, J., De Windt, L., (2002). Chess tutorial and Cookbook (Updated for version 3.0). Eds ENSMP-CIG LHMRD0213.
- Vernoux, J.F., Genter, A., Razin, P., Vinchon, C., BRGM, O., BRGM, N.-P., de, C., 1995. Geological and petrophysical parameters of a deep fractured sandstone formation as applied to geothermal exploitation. *BRGM Rep.* 70, 38622.
- Vidal, J., Genter, A., Schmittbuhl, J., 2015. How do permeable fractures in the Triassic sediments of Northern Alsace characterize the top of hydrothermal convective cells? Evidence from Soultz geothermal boreholes (France). *Geotherm. Energy* 3, <http://dx.doi.org/10.1186/s40517-015-0026-4>.
- Zhu, W., Wong, T.-F., 1997. The transition from brittle faulting to cataclastic flow: permeability evolution. *J. Geophys. Res.* 102, 3027, <http://dx.doi.org/10.1029/96JB03282>.